THE SPATIAL-TEMPORAL SURFACE HEAT TRANSFER/FLOW FIELD FOR A TURBULENT JUNCTION FLOW

Charles R. Smith
Daniel R. Sabatino
Department of Mechanical Engineering and Mechanics
Lehigh University
Bethlehem, PA 18015, USA

Thomas J. Praisner
Pratt and Whitney
400 Main Street
East Hartford, CT 06108, USA

ABSTRACT

A water channel study of the instantaneous and time-mean flow topology for a turbulent junction flow, and the associated endwall heat transfer is presented. A new, temporally responsive test section and film-based imaging process are employed, allowing the simultaneous acquisition of both high-density Particle Image Velocimetry (PIV) and instantaneous endwall heat transfer data using thermochromic Liquid-Crystals (LC). Using this experimental system, the behavior of the junction-region flow structure and consequent surface heat transfer are established for both temporal sequences and time-mean averages. The strong influence of resident, but temporally active, junction region vortices in strongly elevating the local surface heat transfer is clearly demonstrated.

1. INTRODUCTION

When a turbulent boundary layer approaches a bluff-body obstruction, the body-generated adverse-pressure gradient precipitates a separation process which forces the impinging boundary layer vorticity to reorganize into a dominant Horseshoe Vortex (HV) as illustrated schematically in Figure 1. This horseshoe vortex circumscribes the leading edge of the bluff body with legs extending downstream, and is characterized by both significant aperiodic unsteadiness of the vortex, and generation of quasi-periodic eruptions of surface fluid due to vortex-surface interactions (Praisner et al. 1997; Peridier et al., 1991).

Such turbulent junction flows characterize many practical flows, such as wing-fuselage junctions on aircraft, conning tower-body junctions on submarines, and turbomachinery blade-rotor junctions. The heat transfer in turbulent junction flows is of particular interest because the associated flow structures have a profound impact on surface heat transfer in the endwall region of turbine blades. The presence of the HV system has been found to increase the overall heat transfer rate in the endwall region by as much as 300% over surfaces beneath conventional turbulent boundary layers (Hippensteele and Russell, 1988; and Praisner et al., 1997).

In recent years, the primary focus of junction flow studies has been the documentation of the mean flow field. Through

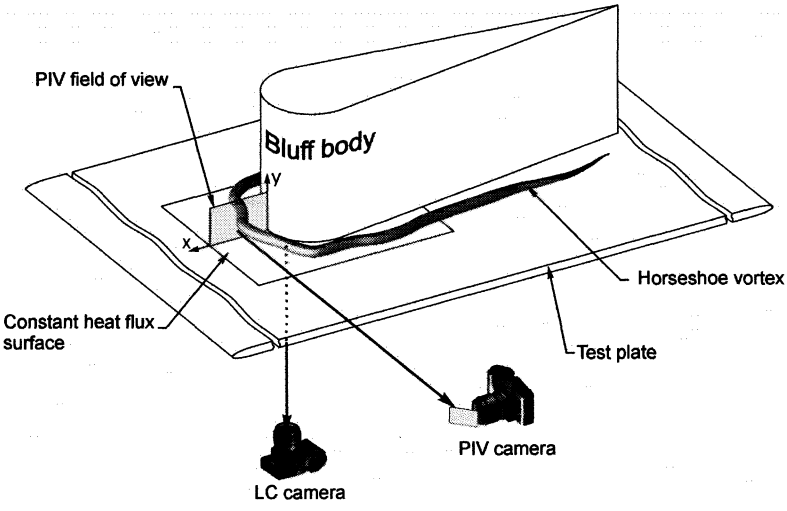

Figure 1. Apparatus employed for temporal acquisition of simultaneous PIV-surface heat transfer.

the use of point-wise velocity measurements and flow visualization studies, the existence of the HV, as well as other sporadically-appearing flow structures, has been documented. As shown in a symmetry plane streamline schematic in Figure 2, the general mean flow structure of a turbulent junction flow consists of a primary vortex [the HorseshoeVortex (HV)], a counter-rotating vortex immediately upstream termed the Secondary Vortex (SV), a separation vortex termed a Tertiary Vortex (TV), and a small vortex in the immediate junction corner termed a Corner Vortex (CV).

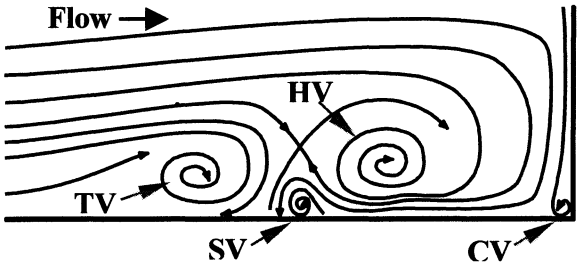

Figure 2. General turbulent junction flow structure

While previous studies have developed some level of agreement regarding time-mean behavior, there are many unresolved issues concerning the salient features of turbulent junction flows and the associated endwall heat transfer. These include: the magnitude and distribution of the heat transfer enhancement in the junction region, the time-mean flow topology, and (most importantly) the mechanisms which give rise to regions of elevated heat transfer. Nearly all research on turbulent junction flow heat transfer has focused on the *time-mean* behavior of both the flow field and the endwall heat transfer. Very little information is available to assess the spatial-temporal behavior of the local flow structure and the associated effect on the local instantaneous heat transfer in the endwall region.

The objectives of the study reported here are to:

- experimentally examine and characterize both the time-mean and the spatial-temporal flow field/heat transfer behavior for a turbulent junction flow, and
- identify the key flow processes causing surface heat transfer enhancement in the endwall region.

2. EXPERIMENTAL APPARATUS

The experimental apparatus employed for this study is designed for use in a free-surface water channel, and is described in detail in Praisner (1998). The key component of the experimental system is a constant heat flux plate, or "insert" plate, which mounts into a larger "test" plate on which the experimental flow conditions are produced. The test plate is designed to allow the attachment of various length boundary layer-development plates.

The primary element of the experimental apparatus is a constant heat flux insert plate (Fig. 3) machined from 3.18 cm thick acrylic (Plexiglas). A shallow rectangular cavity,

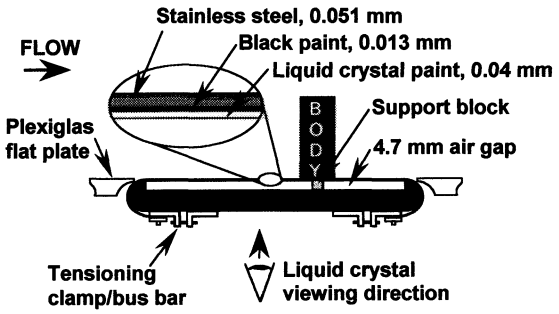

Figure 3. Constant heat flux insert plate

4.7 mm deep by 37.15 cm in the streamwise direction by 33 cm in the cross-stream direction, is machined into the top surface of the insert plate. Using composite bus bar/tensioning clamps, a 0.051 mm thick, type 316 stainless steel foil is stretched tightly around the ends and over the top surface of the insert plate and cavity, as shown in Figure 3. A thin layer of silicon grease applied to the rim of the cavity forms a watertight seal between the plate and the foil, creating an air cavity that imposes an essentially perfect insulating boundary condition on the back side of the foil. A variable, low-voltage (< 6 volts), high-amperage AC power supply is used to galvanically heat the stretched stainless steel foil at heat fluxes of up to 16,000 W/m^2.

Surface temperature sensing is accomplished using thermochromic LCs applied to the non-flow (cavity) side of the resistively-heated stainless steel foil. The LCs, which are viewed from below, are separated from the insert plate by the thin, air-filled insulating cavity, eliminating degradation of the crystals due to water contact and allowing PIV measurements to be done on the flow side of the constant heat flux surface without contamination from the LC light source.

Micro-encapsulated thermochromic LCs (Hallcrest, Inc. type C17-10), with a nominal diameter of 10-15μm, are applied as a slurry of LCs and distilled water onto a black paint undercoating using an airbrush, producing a nominal LC thickness of 40 μm. The color play of the LCs is illuminated obliquely using a modified Kodak slide projector bulb and optics.

The experimental test plate is mounted horizontally in a closed-circuit, free-surface 6000 liter water channel with a 5.0 m long x 0.9 m wide x 0.4 m test section. The channel is capable of a range of flow speeds from 0.01 m/s to 0.4 m/s with ±2% span-wise uniformity and a maximum turbulence intensity of ±0.2%. All bluff bodies are placed directly on the surface of the test plate.

A Nikon F4 35mm camera, with Kodak Elite II 400 color slide film, is used to capture the LC images, which are digitized and converted to temperature fields using a calibration method described in Sabatino et al. (1999). Employing the temperature distributions obtained from the LCs, the convective heat transfer equation is solved to yield high-resolution distributions of the instantaneous heat transfer coefficient, h. The resulting distributions are

ultimately represented as non-dimensionalized local heat transfer coefficients in the form of the Stanton number $[h/(\rho U_\infty c_p)]$.

High image-density PIV (Adrian, 1991; Rockwell et al., 1993) is used to establish the velocity field in conjunction with the surface heat transfer measurements. A film-based PIV technique developed by Rockwell et al. (1993) is employed which uses a scanning 10-Watt laser sheet to illuminate a suspension of neutrally-buoyant, silver-coated spherical particles with a mean diameter of 12 μm and seeding concentration of approximately 2000 particles/cm^3. A second Nikon F4 35mm camera is used to capture the PIV images on Kodak Tmax 400 black-and-white film. A rotating bias mirror is used to correct for directional ambiguity (Rockwell et al., 1993). Computer synchronization of the two cameras allows simultaneous PIV and LC data to be captured at a maximum frame rate of 5 frames/s.

An analytical assessment of the temporal response characteristics of the TLC surface indicates that the the total response time of the surface (from surface temperature change to color response) is less than 7 ms (greater than 140 Hz). A two-dimensional finite-difference numerical analysis indicates that lateral conduction effects caused by the placement of a bluff body on the foil surface bias the surface temperature reading in a region adjacent to the body of less than 4 times the thickness of the stainless steel (51 μm), or 0.2 mm (Praisner, 1998).

The uncertainty of the velocity/temperature measurements were established using standard uncertainty practices (Kline and McClintock, 1953). The mean uncertainty of the LC measurements over the calibration range of 25 - 32 °C is approximately 4.7%, varying between ±3.6% and ±7.9%, with the highest uncertainties occurring at the high temperature limit of the LCs, where they exhibit the lowest sensitivity (Sabatino et al., 1999). The uncertainty of the PIV measurements was estimated to be ±2%, which is supported by Adrian (1991). The total uncertainty in the streamwise alignment of the simultaneous PIV and LC data was established as be ± 1.0% of a typical PIV field of view (Praisner, 1998).

The bluff body junction employed for the studies presented here was a 5:1 tapered Plexiglas cylinder (see Figure 1) with its interior modified to accommodate the optics required for delivery of the PIV laser sheet (see Praisner, 1998, for details). The heat flux was held at 10,500 W/m^2, the free-stream temperature and velocity were T_∞=24.05 °C and U_∞=14.7 cm/s respectively, and the bandwidth of the LCs employed was 7°C. The corresponding boundary layer parameters were: $Re_x=3.20x10^5$, $Re_D=2.44x10^4$, and $Re_{\delta^*}=1.05x10^3$ (based on an equivalent unobstructed turbulent boundary layer at the junction location). For each flow condition, one or more film rolls of thirty-six realizations were recorded, at either 1 f/s for time-averaged results or 5 f/s for temporal response studies.

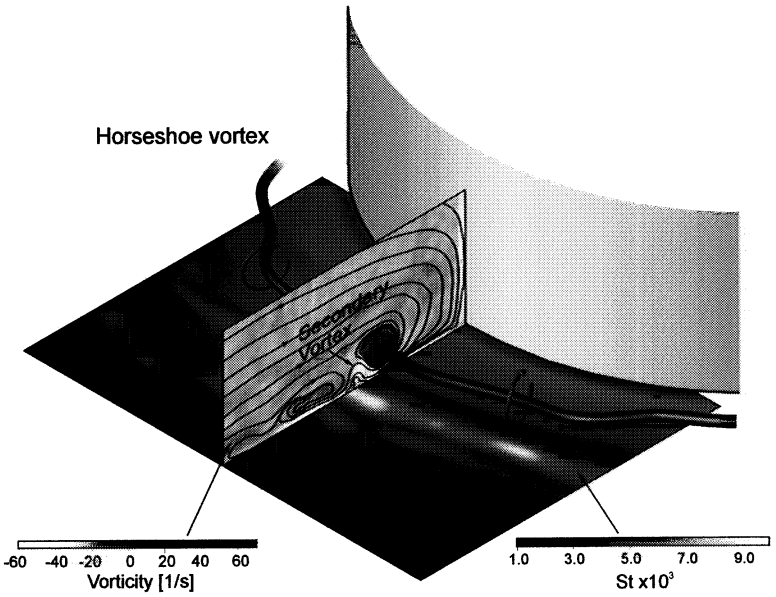

Figure 4. Instantaneous image of simultaneous symmetry plane streamlines/vorticity and endwall Stanton number

3. RESULTS AND DISCUSSION

3.1 Simultaneous PIV and LC Results

In this study, symmetry-plane PIV and endwall heat transfer data were collected simultaneously at 5 f/s. Following post-processing, the instantaneous velocity-based characteristics and corresponding heat transfer properties were established. The simultaneous flow-field and endwall heat transfer data for a selected instant are shown in Figure 4, which is a composite image of instantaneous symmetry-plane vorticity and streamlines juxtaposed with the corresponding instantaneous endwall Stanton number. The general location and rotational sense of the HV are sketched in for reference. This composite image substantiates initial visualization studies, which suggested that the HV resides immediately above a region of relatively low heat transfer, separating two bands of high heat transfer. Figure 4 also illustrates that a transverse region of high heat transfer (light region) upstream of the HV is in fact spatially coincident with the SV, and not the HV. Note that color-enhanced, dynamic sequences of this spatial-temporal behavior, as well as other temporal and time-mean characteristics, can be viewed on the web at www.lehigh.edu/~fluids/main.html.

Figure 5 is a sequence of four instantaneous realizations of *symmetry-plane* flow-field and surface heat transfer results, illustrating the eruptive interaction of the HV with near-wall fluid. In each image, a non-dimensional HV "interaction parameter," suggested by the work of Peridier et al. (1991), is temporally tracked in bar graph form. This interaction parameter, $\Gamma/(aU_\infty)$, is a grouping of the

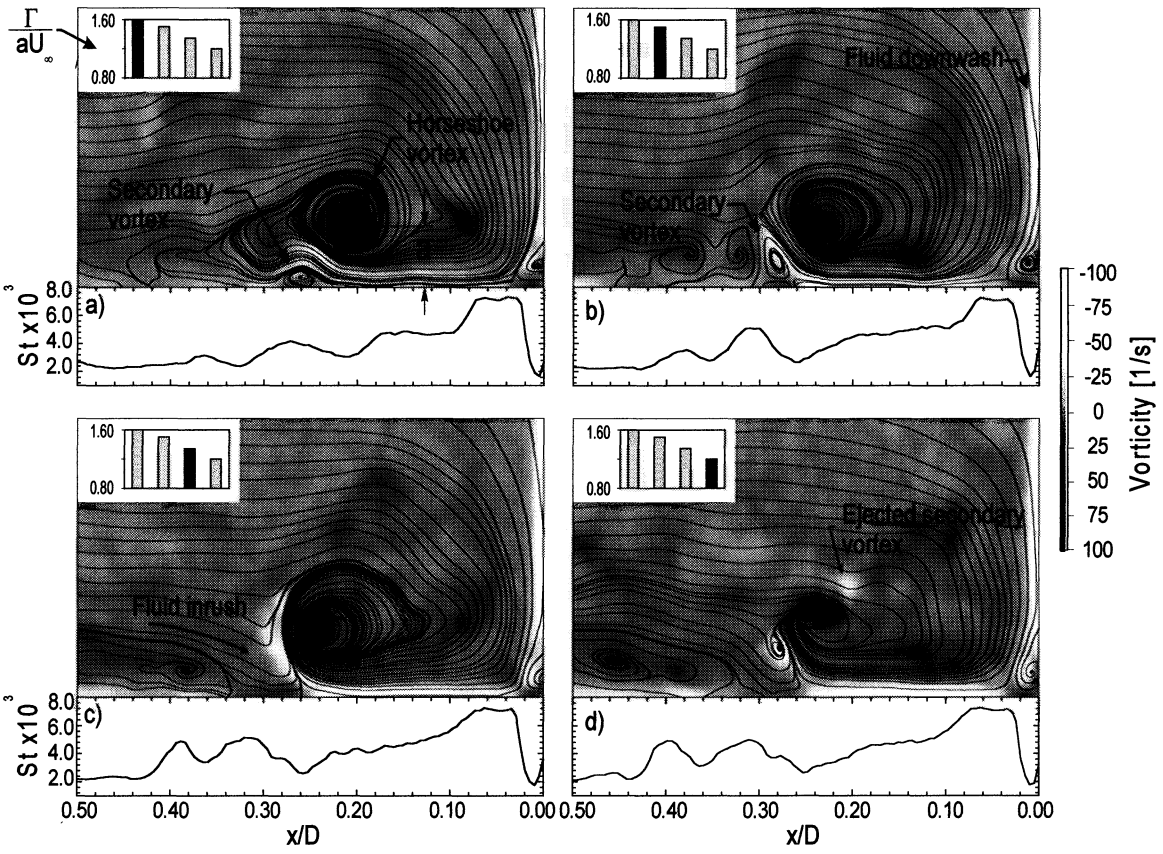

Figure 5. Sequence of four instantaneous realizations of symmetry-plane streamlines/vorticity with corresponding end-wall Stanton number (t=0.2s)

circulation strength of the HV as calculated about a contour of constant vorticity (Γ), the vertical distance from the center of the HV to the endwall (a), and the free-stream velocity (U_∞).

At the beginning of this sequence, the interaction parameter is high, which suggests that conditions are right for the development of a strong vortex-surface interaction, which is indicated in Figure 5a by the development of a secondary vortex (SV) of opposite rotation to the primary horseshoe vortex (HV). As this interaction process continues, a focusing of the SV develops, as shown in Figure 5b, reflected by a corresponding elevation of the surface heat transfer near X/D≅0.30. The source of this elevated heat transfer is revealed in Figure 5c, where the SV ejects from the surface, and is replaced by an inrush of cool fluid from upstream which causes an even broader local elevation of the surface heat transfer. The impact of this inrush of cool fluid appears to be maintained in Figure 5d, with the heat transfer remaining elevated in the vicinity of X/D≅0.30 to 0.40, as the surface fluid associated with the SV migrates up and around the HV.

This process of vortex-boundary layer interaction follows an evolutionary process similar to that described in seminal simulations of vortex-surface interactions by Peridier et al. (1991) and Puhak et al. (1995), among others. Their results indicate that when a vortex is in close proximity to a surface, it stimulates the development of the local boundary layer (due to the vortex-imposed surface pressure gradient), that can rapidly generate a region of unsteady separation, manifested by the appearance of a secondary vortex. Depending on the strength and proximity of the primary vortex, the SV can grow rapidly, resulting in a strong induced up-flow between the primary and secondary vortices (e.g. Figure 5b). Ultimately, the secondary vortex is ejected into the outer flow, which is reflected by local temporal concentrations in the surface heat transfer, essentially identical to the processes illustrated in Figure 5.

Note that the process of vortex/near-wall-fluid interaction shown in Figure 5 was observed to occur six times over three sets of 36 simultaneous/instantaneous realizations taken at 5 fr/s.

3.2 Time-Mean Flow Field and Heat Transfer Results

Figures 6 and 7 show respectively the time-mean results of the endwall heat transfer and symmetry-plane PIV data averaged across the three sequences of 36 images taken at 1 f/s. In Figure 6 the bimodal nature of the heat transfer is reflected by the transverse bands of higher heat transfer that

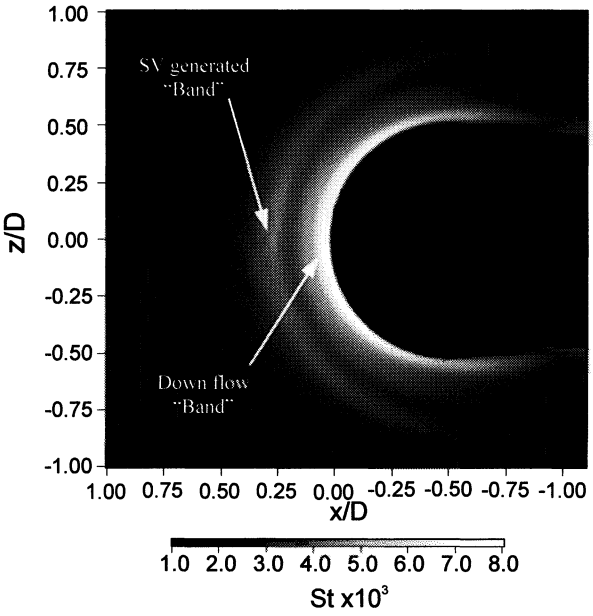

Figure 6. Time-mean endwall Stanton number

extend from the symmetry plane around the leading edge of the tapered cylinder. The band closest to the body is a result of the impinging down flow of cool fluid from the face of the body. Farther removed from the body, a secondary band of high heat transfer develops, which is associated with the generation and unsteady behavior of the SV. The intensity of this secondary band gradually diminishes as the flow moves circumferentially around the body, and away from the symmetry plane.

The peak in the time-mean heat transfer occurs in the corner region of the symmetry plane, and corresponds to an increase of well over 300% above comparable turbulent boundary-layer behavior. This augmentation is substantially higher than the values of roughly 200% reported by Hippensteele and Russel (1988) and Lewis et al. (1994). This variance is felt to possibly reflect the order of magnitude variance between the Reynolds numbers of the present study and the previous investigations.

Figure 7 illustrates the time-mean symmetry-plane flow-field, wall shear, Stanton number, and RMS Stanton number. Note the clear presence of the horseshoe, secondary, tertiary, and corner vortices in the time-mean flow field on the symmetry plane.

The time-mean symmetry-plane horseshoe vortex is characterized by a stable-focus streamline topology at a mean location of x/D≅0.18 and y/D≅0.06 where the boundary layer thickness is 0.34D. While not obvious in the time-mean streamline topology, the existence of a secondary vortex is indicated by a focused region of negative vorticity (light gray region) between the horseshoe and tertiary vortices in Figure 7. The secondary vortex is characterized by a length scale half that of the horseshoe vortex and opposite-sign rotation. A time-mean tertiary vortex is also evident in Figure 7,

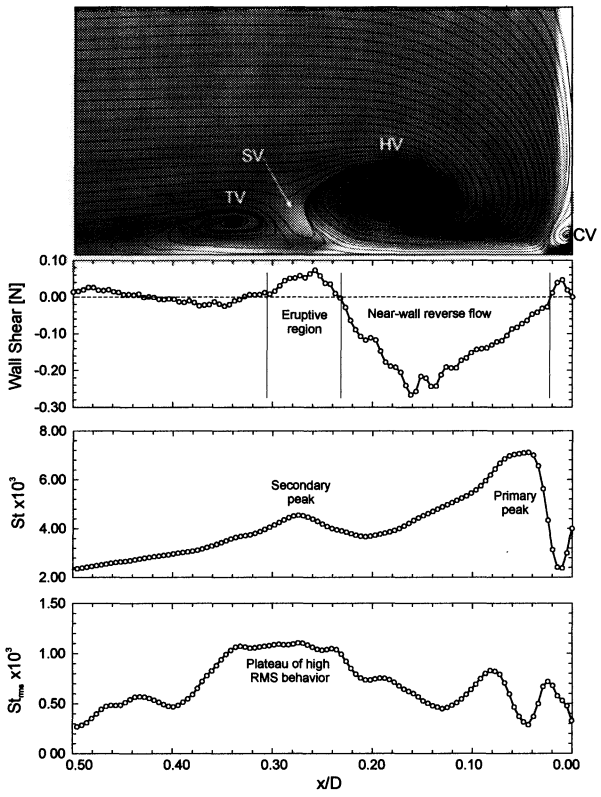

Figure 7. Time-mean symmetry-plane streamline/vorticity behavior with corresponding wall shear, Stanton number, and RMS Stanton number.

indicated by a stable focus of the streamlines and a weak concentration of negative vorticity.

Note that the flow in the corner region (0.0<x/D<0.05) of the symmetry plane is dominated by a small (~25% of the horseshoe vortex diameter) corner vortex that is a stable, relatively steady flow feature. The formation of this corner vortex is the result of a separation-induced roll-up of the boundary layer formed by the down-wash of fluid along the face of the bluff body.

The time-mean symmetry-plane wall shear is shown immediately below the flow-field data in Figure 7. The zero-shear point located at x/D=0.02 corresponds to the stagnation point of the downwash fluid on the endwall. As this downwash fluid turns and is advected upstream by the pressure gradient, the shear stress reaches a negative minimum at x/D=0.16, immediately under the HV. A second point of zero shear occurs at x/D=0.23, corresponding to a separation of the reverse-flow boundary layer beneath the horseshoe vortex. As shown in Figure 7, a small peak in positive shear develops in the vicinity of the secondary vortex, which is coincident with peaks in Stanton number and St_{rms}; in fact, the highest fluctuations in Stanton number are coincident with this region adjacent to the secondary vortex.

The bimodal distribution of the time-mean Stanton number shown in Figure 7 reflects the double bands of high heat transfer discussed above for Figure 6. The largest peak in Stanton number occurs in the corner region of the junction, between $0.00<x/D<0.08$, and reflects a roughly 300% increase over the impinging turbulent boundary layer. The RMS Stanton number behavior associated with this primary peak in Stanton number reflects fluctuations of ±12% about the mean.

A secondary peak in Stanton number develops near $x/D=0.27$, representing over a 200% elevation in Stanton number compared to the impinging boundary layer, and is coincident with the time-mean location of the secondary vortex. The RMS Stanton number for this second peak is approximately ±25%, which is the highest fluctuation in Stanton number encountered for the junction flow.

Note in Figure 7 that the location of the horseshoe vortex coincides with a valley, or local minimum, in Stanton number between the bimodal peaks. This development of a local Stanton number minimum adjacent to the reverse-flow boundary-layer separation point is consistent with the computational results reported by Puhak et al. (1995) for a laminar junction-type flow.

4. CONCLUSIONS

The turbulent junction region is dominated by a primary horseshoe vortex that circumscribes the base of the bluff body with legs that trail downstream. The flow of cool outer-region fluid down the face of the bluff body results in a primary peak in Stanton number very near the body. The subsequent interaction of the HV with the surface fluid causes the aperiodic generation and ejection of secondary vortices upstream of the HV, which result in a consequent second peak in Stanton number and a high degree of flow and thermal unsteadiness.

The process of generation and ejection of secondary vortices helps precipitate broad temporal variations in Stanton number, particularly near the formation site of secondary vortices. These fluctuations appear to be a result of both the removal of warm surface fluid by the vortex ejection process, complemented by the corresponding influx of cool fluid from upstream.

5. REFERENCES

Adrian, R.J., 1991, "Particle-imaging techniques for experimental fluid mechanics," *Annual Review of Fluid Mechanics*, Vol. 23, pp. 261-304.

Hippensteele, S.A., and Russell, L.M., 1988, "High resolution liquid-crystal heat-transfer measurements on the end wall of a turbine passage with variations in Reynolds number," NASA Technical Memorandum 100827.

Kline, S.J., and McClintock, F.A., 1953 "Describing Uncertainties in Single-Sample Experiments," *Mechanical Engineering*, pp. 75:3-8.

Lewis, D.J., Simpson, R.L., and Diller, T.E., 1994, "Time-resolved surface heat flux measurements in the wing/body junction vortex," *Journal of Thermophysics and Heat Transfer*, Vol. 8, No. 4, pp. 656-663.

Peridier, V.J., Smith, F.T., and Walker, J.D.A., 1991, "Vortex-induced boundary layer separation Part 1. The unsteady limit problem $Re\rightarrow\infty$," *Journal of Fluid Mechanics,* Vol. 232, pp. 99-131.

Praisner, T.J., Seal, C.V., Takmaz, L., Smith, C.R., 1997, "Spatial-temporal turbulent flow-field and heat transfer behavior in end-wall junctions," *International Journal of Heat and Fluid Flow*, Vol. 18, No. 1, pp. 142-151.

Praisner, T.J. 1998, "Investigation of Turbulent Juncture Flow Endwall Heat Transfer and Fluid Flow," Ph.D. Thesis, Lehigh University, Dept. of Mech. Engrg. & Mech.

Puhak, R.I., Degani, A.T., and Walker, J.D.A., 1995, "Unsteady separation and heat transfer upstream of obstacles," *Journal of Fluid Mechanics*, Vol. 305, pp. 1-27.

Rockwell, D., Magness, C., Towfighi, J., Akin, O. and Corcoran, T., 1993, "High image-density particle image velocimetry using laser scanning techniques," *Experiments in Fluids*, Vol. 14, pp.181-192.